The turbulent structure of the flow field generated by a hydrofoil in stalling condition beneath a water–air interface

Sandro Longo [a,*], Francisco M. Domínguez [b], Alessandro Valiani [c]

[a] Department of Civil Engineering, University of Parma, Parco Area delle Scienze, 181/A, 43124 Parma, Italy
[b] Grupo de Investigación de Dinámica Fluvial e Hidrología, Universidad de Córdoba, Spain
[c] Department of Civil Engineering, University of Ferrara, Via Saragat, 1, 44122 Ferrara, Italy

A B S T R A C T

In this paper, measurements beneath the interface of the flow past a hydrofoil in water during stalling conditions are used to characterise the flow field and to extract and to analyse the small eddies using an original algorithm based on the wavelet transform. The detected eddies are analysed to evaluate their spatial distribution and their intensity separating the wake of the foil-related from the wake of the breaker-related eddies. The wake of the foil-related eddies have an almost symmetric distribution of circulation with slight dominance of counter-clockwise (CCW) eddies, while the breaker-related eddies have an asymmetric distribution of circulation, and clockwise (CW) eddies are dominant. The joint probability density function (PDF) of the turbulent kinetic energy (TKE) and the Reynolds shear stress is computed by referring to the time-averaged values in the area occupied by the eddies. A similar PDF computed using the instantaneous values during eddies presence shows values of TKE and Reynolds shear stress roughly twice the average values, i.e., eddies can be associated to larger fluctuations of the flow field respect to the time average flow field. However, on average, the Reynolds shear stress during eddy presence is less than the Reynolds shear stress of the time-averaged flow at the same location. The sign of the Reynolds shear stress is systematically opposite to the time-averaged value in quadrants Q2–Q4 for CW eddies and in quadrants Q1–Q3 for CCW eddies. Therefore, in the presence of eddies there is a counter-flux of momentum. The conditional analysis of the terms of the TKE balance indicates that, in the wake of the foil and during the presence of eddies, the production is ≈15% stronger than the time-averaged production at the same location occupied by the eddies. Beneath the free surface the production is ≈30% weaker than the time average. A similar analysis for the advection indicates that, in the wake of the foil, the advection in the presence of eddies is an order of magnitude greater (in absolute value) than the advection due to the time-averaged flow at the same location. Additionally, beneath the free surface, the advection in the presence of eddies is much greater than the average. A similar behaviour can be observed for the transport term due to turbulence. Therefore, in the presence of eddies, production plus advection plus transport is enhanced with respect to the average flow and is increased approximately by 40% in the wake of the foil and 20% beneath the free surface.

1. Introduction

The wake past hydrofoils and airfoils has been widely studied and has received the attention of many researchers due to the practical implication in several fields. In addition to the classical use in airplanes as wings and in screws, hydrofoils are used to mix fluids and to enhance oxygenation or chemical exchange or mixing in industry and in waste water treatment installations. The efficiency of hydrofoils within these specific applications is measured by several parameters, amongst them the ability to generate turbulence at difference scales, to enhance convection and to increase turbulent diffusion. Coherent structures are considered very important in turbulent exchanges. For a jet in the far field, it is estimated that 10% of the total energy is contained in coherent structures [2], while for mixing layers, they account for 20% [13]. Existence of coherent structures in most physical flow fields is widely documented and eddies are only one of the numerous items of the list. Sweep, ejection, streaks in turbulent layer are also coherent structures, with a further categorisation into 'spots', 'slugs' and 'puffs' proposed according to some specific properties [41]. Spatial and/or temporal coherence is an important notion

* Corresponding author.
  E-mail address: sandro.longo@unipr.it (S. Longo).

Nomenclature

$\overline{\cdots}$	time average, space average operator
$\widetilde{\cdots}$	symbol for wavelet coefficient
$\widehat{\cdots}$	conditional average operator in presence of eddies
$\cdots *$	computed value
α	angle of attack, angle of the mirror, energy coefficient
Γ	circulation of the vortex
Δ	variable in Chong et al. [7] criterion
$\varepsilon_{(\cdots)}$	uncertainty, absolute value
η	transverse non dimensional coordinate for the wake
κ	turbulent kinetic energy
λ_2	intermediate eigenvalue in Jeong and Hussain [20] criterion
v	kinematic viscosity
ρ	mass density
σ	parameter of the size of a vortex
$\sigma_{(\cdots)}$	uncertainty, relative value
$\Phi(\cdots)$	wavelet transform
χ^2	function
ω_z	component of vorticity in the spanwise direction
$\boldsymbol{\Omega}$	vorticity tensor
A, A_i, A_e	advection of TKE, components of advection, advection of TKE if eddies are present
a	dilation parameter in wavelets
b	parameter
C	cord length, concentration, coefficient
CW, CCW	clockwise, counter-clockwise vortex
d	water depth upstream of the airfoil
dT	interval time between two coupled frames in PIV
f_{acq}	frequency of acquisition
FOV	Field Of View
Fr	Froude number
h	trailing tip elevation respect to the bottom of the flume
i_f	bottom inclination
L_0	transverse length scale of the wake
P, P_{ij}, P_e	production of TKE, components of production, production of TKE if eddies are present
PDF	probability density function
PIV (DPIV)	Particle Image Velocimetry (Digital)
PID	Proportional–Integral-Derivative feedback system
PMMA	polymethil methacrilate
q^2	twice the turbulent kinetic energy per unit mass
Q	water discharge, variable in Hunt et al. [18] criterion
Re	Reynolds number, based on the cord length and on kinematic viscosity
r, r_v	radial distance
r_e	radius of the eddy
$\boldsymbol{S}, S_{ij}$	tensor of strain rate
s_{ij}	fluctuating tensor of strain rate
t	time
T, T_{ij}, T_e	transport of TKE, components of transport, transport of TKE if eddies are present
TKE	turbulent kinetic energy
U_0, U_s	asymptotic upstream velocity, defect velocity
U, V	streamwise, transverse velocity
U', V'	streamwise, transverse fluctuating velocity
x, y	spatial co-ordinates
X_W	horizontal size of the interrogation window

for coherent structures and is often used to build a detection function. In the present paper we mainly analyse the coherent structures and eddies generated by the hydrofoil positioned beneath an air–water interface, focussing the attention to the small size eddies.

Despite the simplicity of the structure of an eddy, its mathematical definition and detection is a challenging task. In the case of stable, large eddies, the correlation function and the spectrum are useful tools to detect their size and intensity, but if eddies are subject to a random motion or have a wide range of length scales (as happens in most flows), their effects are less detectable.

The definition of an eddy is itself ambiguous. The early definition by Lugt [27] considers a vortex as a 'multitude of material particles rotating around a common centre'. The simplest definition of a vortex is most likely given by Robinson et al. [34] and has also been practically adopted by Agrawal and Prasad [2] and others: the streamlines of a vortex look roughly circular or spiral in a reference point moving with the core; hence, it is necessary to look for these patterns in the instantaneous flow. For this aim, it is first necessary to remove the low frequency components, which include the mean motion and can be orders of magnitude stronger than the vortices. In some flows, a high-pass filtering technique has been successful [1,2], and some conditional-sampling techniques have been suggested [3,19]; however, these techniques are less efficient in fully turbulent flows (e.g., far-field of jets, wakes, mixing layers), which require the knowledge of instantaneous vorticity fields. Additionally, the vorticity magnitude fails in separating vortices from shear flows, and other algorithms based on a proper orthogonal decomposition that allow for the isolation of the most energetic modes, which are followed by different criteria for identifying a vortex (such as the monotonicity of velocity along a circular path in the flow field, e.g., [37]), require numerous thresholds.

Two-dimensional Digital Particle Image Velocimetry (DPIV) is a tool designed to detect vortices compared with other point-wise techniques, but the process of identifying the vortices is still not completely objective. Among the approaches, which give the criteria to identify a vortex, a distinction should be made between *local* and *non-local* approaches. Amongst the numerous authors suggesting local approaches, which use only local variables, we mention [32,19,18] (Q criterion); [30,40,7] (Δ criterion); [20] (λ_2-criterion); [43] ('swirling strength' criterion); [16,5].

Non-local approaches often use local variables but also verify the existence of a spatial coherence inside the possible eddy. A non-local approach proposed by Cucitore et al. [8] introduces a measure of the coherence inside a possible eddy in conjunction with the Δ criterion. Another non-local approach for a three-dimensional flow is reported in Chakraborty et al. [9] and uses the Δ criterion to verify that the orbits of the material points inside the vortex core were compact as well.

The concept of Galilean invariance has been customarily used as starting point for many of these criteria. However, as documented by Haller [17], it is not a sufficient property for all flows, and instead, objectivity should be mandatory in rotating flows and for flows with interacting vortices. An exact local objective criterion is reported in Tabor and Klapper [38], who elaborated on a version of the Q criterion that is able to guarantee that fluid particles inside the vortex move yet form an impenetrable swirling region in a two-dimensional flow. The generalisation to three-dimensional flows is known as the $\boldsymbol{M}_Z$ criterion given by Haller [17], which his based on Lagrangian stability considerations.

Unfortunately, all these sophisticated criteria are primarily based on topology considerations and are difficult to implement in the analysis of the experimental or numerical data because experimental uncertainties and numerical errors may give

completely incorrect results. In addition in most cases they rely on three dimensional measurements in several points at the same time, which only recently are becoming available for laboratory measurements. For this reason, a simple criterion that can be correct for a specific flow is often preferred to a general more complex criterion that is difficult to apply due to the lack of flow field information.

The flow field analysed in the present paper is shown in Fig. 1, with two photographs with the wake of the foil visualised using methylene blue injected by a needle to enhance the coherent structures. The hydrodynamics of foils near a free surface has been widely studied from a numerical and experimental point of view since the hydrofoils are often used as stabilizer in submarines or are essential components in the design of fast boats. The early numerical computations based on a potential flow theory are due to Giesing and Smith [15], progressively extended to include turbulence modelling and cavitation effects (e.g., [35]). Also several experiments were performed on pressure distribution around the hydrofoils [31], which gave the essential information to compute the lift and the performances of the hydrofoils, or direct measurement of the lift at full scale [11].

The wake of the foils is surrounded by the upper lobe, near the free surface, and the lower lobe. The wake is the domain where there is a defect velocity respect to the incoming stream, the two labels mark the transition from the core of the wake to the external flow. The spilling breaker (similar to a hydraulic jump) is evident downstream and generates a wake near the free surface.

In this paper, we use DPIV techniques to analyse the flow field past the hydrofoil and near the free surface and to extract the small eddies. According to this definition, the analysed eddies are much smaller than the length scales imposed by the geometry of the system, like the cord length of the hydrofoil and the length scale of the wake. At the same time the experimental apparatus limits the minimum size of the detected eddies, which are always larger than the energy dissipating eddies. Despite t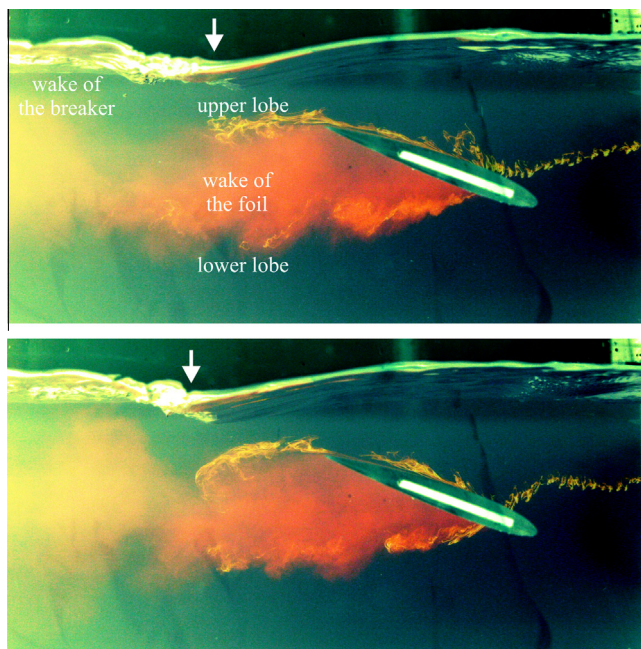he high resolution of the video camera, we could not cover all the field of interest, which is elongated and extends for several cord lengths downstream; to balance the need of a good spatial resolution of the extracted data and the opportunity to cover all the wide region of the flow field of interest, we decided to conduct a series of measurements in identical conditions to collect a mosaic of individual frames. Because each frame (or series of frames) is a realisation and because each realisation is inherently different, specific attention was paid to build up the flow statistics through ensemble averaging.

The paper is organised as follows. After the description of the experimental set-up in Section 1, Section 2 introduces the techniques for eddies eduction, and Section 3 is devoted to the statistics of the eddies. Section 4 describes the quantification of the effects of the eddies in terms of the TKE balance equations. The conclusions are reported in the final section.

Some relevant aspects of the flow field are detailed in [26], devoted to different analyses of the same flow field.

2. Experimental set-up

The experiments were conducted in the flume in the Laboratory of Hydraulics of the Department of Civil Engineering (DICATeA) of the University of Parma, Italy. The flume is 0.30 m wide, 0.45 m high and 10 m long; the sidewalls are made of glass, the bottom is stainless steel and a flow straightener at the entrance eliminates the large-scale vortices and eddies. A bottom-hinged flap gate at the downstream end of the flume allows for water level control. The flow rate is measured by a Promag Hendress-Hauser magnetic flowmeter, with an accuracy of 0.5% of the instantaneous measured value and the discharge in the flume is controlled through a PID regulator.

The Reynolds number of the water stream, which is based on the hydraulic radius, is equal to 38 900, and the Froude number is Fr = 0.26; hence, the water flow is turbulent and is in a subcritical regime. The measured free stream turbulence in the midsection of the flume is equal to 5%. The water used in the experiments is tap water seeded with silt, which has a size of 10–20 μm, to facilitate the subsequent acquisition of information using the DPIV. The specific weight of silt is ≈1.9 but the free surface forces are dominant for the small particles used in the experiments and prevent a fast sedimentation. The NACA profile belongs to the four digit series 6024, is asymmetric and is achieved using polymethyl methacrylate (PMMA) with a milling machine. The struts that support the hydrofoil are close to the two side walls and are of minimum impact, since the pattern of disturbances at the free surface due to their presence does not reach the measurement plane. Measurements were carried out using a TSI PIV with a 2048 × 2048 pixel video camera (TSI Power View Model 630149) fitted with a Nikon NIKKOR AF D 50 mm/f lens with an adaptor ring (Nikon PK-12), which increases the focal by 14 mm. The calibration of the PIV gave a resolution of 0.11 mm per pixel. The light source was a water cooled Solo Nd:YAG III dual laser head with maximum output energy of 50 mJ. The acquisition frequency for an image couple was 3.75 Hz with a time interval between the two images of 2000 μs. The layout is shown in Fig. 2.

We choose the solution of moving the hydrofoil leaving in place the PIV assembly (mirror, laser, video camera) in order to minimise the errors in the geometry set-up. The channel is long enough to guarantee that a different position of the hydrofoil (the hydrofoil has been moved upstream 150 mm in each of the four sets, i.e., 450 mm in total which is less than 5% of the length of the channel) does not affect the incoming flow characteristics. It is equivalent to assume that the flow in the channel is truly homogeneous in the range spanned by the hydrofoil.

Near the free surface, the computation of velocity was performed by masking the air side. The computation of vorticity
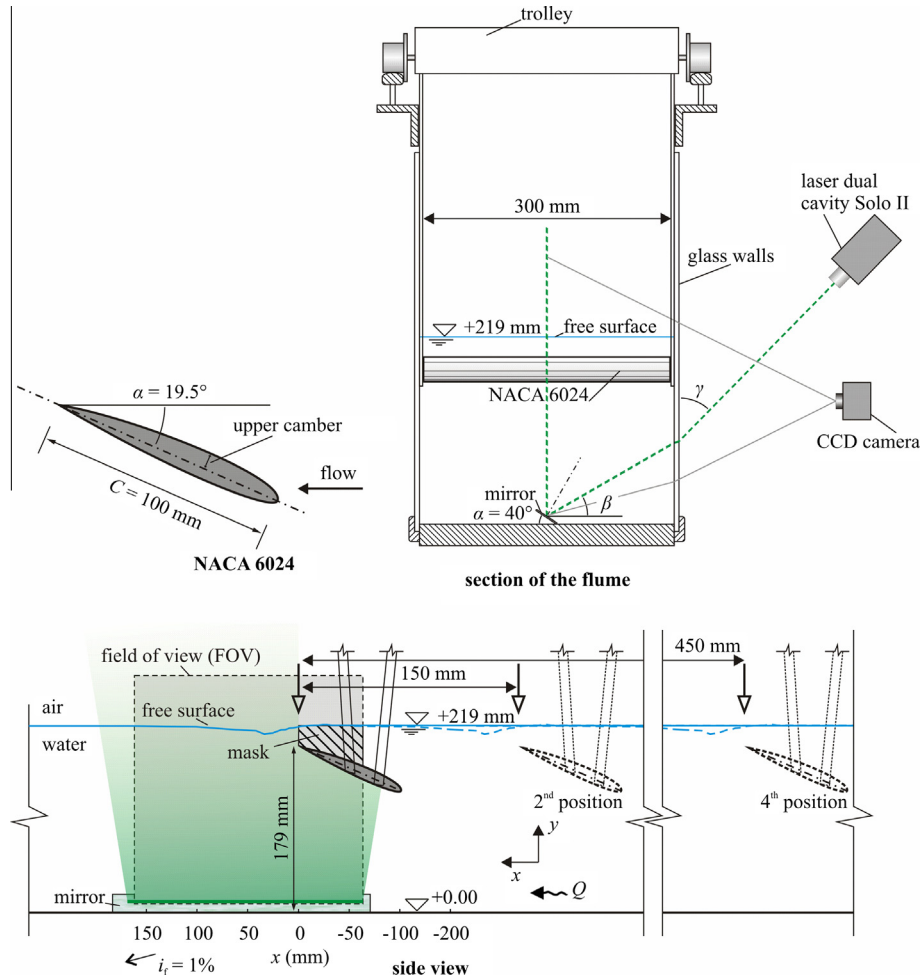

Fig. 1. Two photographs of the hydrofoil with the wake visualised using methylene blue injected on the right side. The hydraulic jump is evident on the left. The time interval between the two frames is 0.33 s. Re = 44 500 and α = 19.5°. (For interpretation of the references to colour in this figure legend, the reader is referred to the web version of this article.)

Fig. 2. An overview of the experimental system.

also required the insertion a constant velocity in the vertical direction that is equal to the first value recorded in the water. This procedure is necessary to avoid a false shear layer at the interface. The computed velocity is phasic averaged, i.e., only refers to the time interval in which water is present.

The detailed analysis of uncertainty for the present tests is reported in Longo et al. [26]. The estimated uncertainty in the velocity is equal to $\sigma_u = \pm 4.1\%$ for the instantaneous value and is equal to $\sigma_u = \pm 1.6\%$ for the averaged value (1000 frames). The spatial derivatives were calculated using a central scheme with an absolute uncertainty of $\varepsilon_{\partial u/\partial x} = \pm 0.7 \varepsilon_u/\Delta x$ [33], where ε_u is the absolute velocity uncertainty and Δx is the interval between the data ($\Delta x = 1.77$ mm in the present tests). For a velocity of 0.38 m/s the uncertainty on the instantaneous derivative is $\varepsilon_{\partial u/\partial x} = \pm 6.1$ s^{-1} and on the instantaneous vorticity is $\varepsilon_{\omega_z} = \pm 12.2$ s^{-1}; the uncertainty on the derivative of the mean velocity is $\varepsilon_{\partial \bar{u}/\partial x} = \pm 2.35$ s^{-1} and on the mean vorticity is $\varepsilon_{\bar{\omega}_z} = \pm 4.7$ s^{-1}.

In addition to the PIV quantitative approach, qualitative information was gained by flow visualisation and acquisition of the image with a digital camera and a digital HD video camera.

The velocity measurement domain is $181 \times 145 \times 1$ mm^3 (W, H, D) in each Field Of View (FOV) and the experiment herein analysed included four subsequent FOVs with an overlap of 31 mm. The mean flow field shows a classical wake past the hydrofoil with two lobes defined upper lobe (near the free surface), and lower lobe (near the bottom of the flume). Table 1 shows the experimental parameters for the tests.

Attention was paid to overcome the problems arising from bubble presence near the free surface, where a breaker develops. Some measurements of fluid-bubble velocity were taken with an Ultrasound Velocity Profiler (e.g., [23]) and compared with the DPIV measurements (not shown).

3. The detection of the eddies

The algorithm developed for the detection of the eddies is based on wavelet analysis. Wavelet analysis is a frequently used tool for turbulence, and an extensive review of wavelet transforms and their application to fluid dynamics can be found in Mallat [28], Meneveau [29], Farge [12] and Longo [22,24]. In the present analysis, we use a simple Mexican hat wavelet defined as

$$\varphi_{a,\xi}(\mathbf{x}) = \frac{1}{a}\varphi\left(\frac{\mathbf{x}-\xi}{a}\right) = \frac{1}{a}\left(2 - \frac{|\mathbf{x}-\xi|^2}{a^2}\right)\exp\left(-\frac{|\mathbf{x}-\xi|^2}{2a^2}\right). \quad (1)$$

The idea behind the present approach is inspired by the analysis conducted by Farge [12] and subsequently extended by several other researchers (e.g., [36,21]). First, we select the vorticity instead of the velocity field to handle a Galilean invariant quantity without the necessity of separating the random field and the uniform motion. It is assumed that a Lamb–Oseen vortex well approximates the vorticity distribution in a cross-section of a three dimensional vortex. Assuming that a series of Lamb–Oseen vortices approximate the vortex distribution in coherent structures is a working

Table 1
Experimental parameters. d is the water depth upstream of the hydrofoil, h is the trailing tip elevation respect to the bottom of the flume, U_0 is the asymptotic velocity, α is the hydrofoil attack angle, Re = U_0C/ν is the Reynolds number based on the cord length C = 100 ± 1 mm, f_{acq} is the frequency of acquisition of the PIV, dT is interval time between the two coupled frames.

d (mm)	h (mm)	U_0 (m/s)	α (°)	Re	f_{acq} (Hz)	No frames	dT (μs)
219 ± 1	179 ± 1	0.381 ± 1.5%	19.5	45 500	3.75	1000	2000

assumption. In reality the model is rigorously valid only for isolated trailing vortices when the flow is dominated by viscosity. In fact, multiple Lamb–Oseen vortices are not a solution of the Navier–Stokes equation and the presence of surrounding vorticity limits the reliability of the Lamb–Oseen vortices in fitting the real vortices.

In a Lamb–Oseen vortex in cylindrical coordinates, the radial velocity is zero, and the tangential velocity is equal to

$$v_\theta(r) = \frac{\Gamma}{2\pi r}\left[1 - \exp\left(-\frac{r^2}{2\sigma^2}\right)\right], \qquad (2)$$

where Γ is the vortex circulation and σ is a parameter of the size of the vortex. The tangential velocity is zero in the axis and has a maximum at a distance $r = 1.58\sigma$.

The vorticity component along the vertical axis decays exponentially, has a maximum in the axis of the vortex and is related to the circulation through the following expression:

$$\omega_z(r) = \frac{\Gamma}{2\pi\sigma^2}\exp\left(-\frac{r^2}{2\sigma^2}\right). \qquad (3)$$

Vorticity value reduces to 95% of the maximum at a distance $r = 2.45\sigma$ from the axis. Because the detection algorithm adopts a wavelet transform, a relationship between the scale of the wavelet and the nominal radius of the Lamb–Oseen, which is adopted as prototype of the vortices to be detected, is necessary. The continuous wavelet transform used in the present analysis relates the vorticity, as in Kim et al. [21], whereas other analyses refer to enstrophy [36]. Assuming a wavelet centred in the eddy, the wavelet transform of the vorticity in cylindrical coordinates is

$$\Phi_{a,0}|\omega = \int_0^{2\pi}\int_0^\infty \omega_z(r)\varphi_{a,0}(r,a)r\,dr\,d\theta = \frac{2\Gamma a^3}{(a^2+\sigma^2)^2}. \qquad (4)$$

The maximum value of the function in Eq. (4) occurs at $a = \sqrt{3}\sigma$; hence, the nominal radius of the vortex is assumed to be $r_e \equiv r|_{\max(v_\theta)} = 1.58\sigma$ or $r_e = 0.91a$.

The effects of the presence of a vortex in the flow field decay relatively fast, and the wavelet transform of the result has a decreasing value in the neighbouring points. Nevertheless the non-zero values in the neighbouring points could be incorrectly identified as distinct vortices, and an algorithm is required to identify possible shadow eddies belonging to the same main eddy. To overcome this problem, a procedure was set up and tested on a synthetic flow field containing vortices: (1) a threshold of the wavelet transform is fixed and only points with a value of the wavelet transform above the threshold are considered; (2) only points where the λ_2-criterion ($\lambda_2 < 0$, where λ_2 denotes the intermediate eigenvalue of the symmetric tensor $\mathbf{A} = \mathbf{S}^2 + \mathbf{\Omega}^2$, where $\mathbf{S}$ is the rate of strain tensor and $\mathbf{\Omega}$ is the vorticity tensor [20]) is satisfied are considered for further analysis; (3) the potential vortices are determined if they have neighbouring points with a transform value still above the threshold, and the patterns of connected points are considered as a potential single vortex. As a first attempt, the axis position (x_C, y_C), the circulation Γ and the value of σ are estimated as weighted averages of the contributions of the connected points; (4) the values of the parameters Γ, a, σ, x_C and y_C are evaluated through a best fitting procedure starting from the first attempt values.

We will measure a generally decreasing vorticity for smaller eddies, the opposite of what we expect. This is the spatial filter

effect due to PIV (and common to all the measuring instruments), which reduces the computed vorticity of the small eddies. A deterministic criterion, like the λ_2-criterion, is necessary to avoid uncertainties in the detection of the coherent vortex structures, otherwise difficult to detect in a context where energy transfer amongst scales is a relevant back ground signal.

The best fitting procedure is set up as explained in the following. The transfer function at a distance r_v of a Lamb–Oseen vortex at the origin is

$$\Phi_{a,0}(\Gamma, \sigma, r_v) = \int_0^{2\pi}\int_0^\infty \frac{\Gamma}{2\pi\sigma^2}\exp\left[-\frac{(r-r_v)^2}{2\sigma^2}\right]$$
$$\times \frac{1}{a}\left(2 - \frac{r^2}{a^2}\right)\exp\left(-\frac{r^2}{2a^2}\right)r\,dr\,d\theta$$
$$= \frac{2\Gamma a^3}{(a^2+\sigma^2)^2}\exp\left(-\frac{r_v^2}{2\sigma^2}\right)\left(1 - \frac{1}{2}\frac{r_v^2}{a^2+\sigma^2}\right), \qquad (5)$$

which for $r_v = 0$, collapses to Eq. (4). By symmetry, Eq. (5) also represents the wavelet transform at the origin for a vortex with axis at distance r_v from the origin. The optimal vortex is obtained by minimising the function

$$\chi^2 = \sum_{j=1}^{N_k}\sum_{i=1}^{N}\left[\Phi_{a_i,0}(\Gamma, \sigma, r_{vj}) - \Phi^*_{a_i,0,j}\right]^2 \equiv f(\Gamma, a, \sigma, x_C, y_C), \qquad (6)$$

where the symbol * indicates the computed values of the wavelet transform of the vorticity field with a zero value of the translation and a scale a_i. The sum is extended to all the scales ($i = 1, 2, \ldots, N$) and to all the connected points ($j = 1, 2, \ldots, N_k$). The necessary condition for a minimum of Eq. (6) is a complicated function that does not have a known analytical solution, and the most effective solution is a trial and error procedure varying the five parameters (Γ, a, σ, x_C and y_C) over a range centred at the first attempt values. The computations were performed in Matlab$^{\circledR}$ with the use of multidimensional arrays. To verify the effectiveness of the approach and of the algorithms, a synthetic velocity field generated with two Oseen eddies and a shear layer was analysed. This synthetic velocity field has the following velocity components:

$$U = \frac{\Gamma_1(y-y_{C1})}{2\pi\left[(x-x_{C1})^2+(y-y_{C1})^2\right]}\left[1 - \exp\left(-\frac{(x-x_{C1})^2+(y-y_{C1})^2}{2\sigma_1^2}\right)\right]$$
$$+ \frac{\Gamma_2(y-y_{C2})}{2\pi\left[(x-x_{C2})^2+(y-y_{C2})^2\right]}\left[1 - \exp\left(-\frac{(x-x_{C2})^2+(y-y_{C2})^2}{2\sigma_2^2}\right)\right]$$
$$+ 2U_s\tanh\left(\frac{y-y_s}{2\delta_s}\right), \qquad (7)$$

$$V = \frac{\Gamma_1(x-x_{C1})}{2\pi\left[(x-x_{C1})^2+(y-y_{C1})^2\right]}\left[1 - \exp\left(-\frac{(x-x_{C1})^2+(y-y_{C1})^2}{2\sigma_1^2}\right)\right]$$
$$+ \frac{\Gamma_2(x-x_{C2})}{2\pi\left[(x-x_{C2})^2+(y-y_{C2})^2\right]}\left[1 - \exp\left(-\frac{(x-x_{C2})^2+(y-y_{C2})^2}{2\sigma_2^2}\right)\right], \qquad (8)$$

$$\omega_z = -\frac{\Gamma_1}{2\pi\sigma_1^2} \exp\left(-\frac{(x-x_{C1})^2 + (y-y_{C1})^2}{2\sigma_1^2}\right) - \frac{\Gamma_2}{2\pi\sigma_2^2}$$
$$\times \exp\left(-\frac{(x-x_{C2})^2 + (y-y_{C2})^2}{2\sigma_2^2}\right) - \frac{U_s}{\delta_s} \operatorname{sec} h^2\left(\frac{y-y_s}{2\delta_s}\right), \quad (9)$$

where $y_s = -70$ mm is the axis of the shear layer parallel to the x-axis, $U_s = 1$ mm/s is the velocity scale of the shear layer and $\delta_s = 1$ mm is the nominal thickness of the shear layer. A random noise has been added to simulate random errors that typically occur in PIV measurements. Fig. 3 shows the velocity fields and the two clusters detected by the algorithms. The results of the optimisation procedure are shown in Table 2, where a very good comparison is reported amongst the evaluated and the imposed parameters of the eddies, even in presence of the added random noise.

In some cases, the function in Eq. (6) has no minimum in the intervals evaluated for the five variables; hence, the candidate eddy is not considered in the subsequent statistics.

This method is similar to the method used by Carlier and Stanislas [6], and the main difference lies in the fact that the authors used the velocity field instead of the vorticity field; hence, they had to introduce a convection velocity of the vortex as an additional parameter for the optimisation.

The choice of the threshold influences the number of eddies detected. If the threshold is too low, the clusters of potential eddies becomes larger, being limited only by the λ_2 criterion and the potential eddies merge in single very large eddies; if the threshold is too high, only a limited number of energetic eddies is detected, generally of very small size. In the present test the threshold is chosen in order to have eddies smaller than 20% of the geometric transverse length scale of the wake immediately past the hydrofoil. This geometric transverse scale, estimated by the analysis of the mean flow, is equal to ≈ 50 mm (half the cord length). Hence the maximum size of the eddies included in the present analysis is ≈ 10 mm and the threshold in the wavelet transform has value $0.32U_0$, detected by a trial and error procedure.

4. The description of the flow

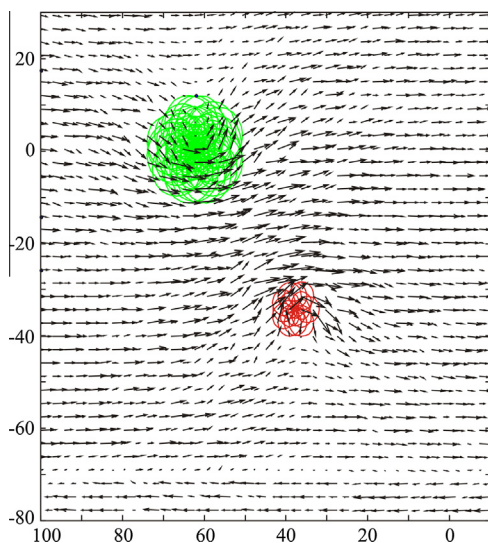We are dealing with a hydrofoil inserted in the uniform flow field which generates a wake downstream. The wake is not

Fig. 3. The velocity field obtained by imposing two Oseen vortices with opposing vorticity and a shear layer plus a random noise. The circles are the eddies in clusters as detected by the algorithm.

Table 2
Comparison between the synthetic eddy characteristics and the values detected by the optimisation procedure.

	x_C (mm)	y_C (mm)	Γ (mm²/s)	σ (mm)
Imposed	−37.86	−34.39	100	2.0
Evaluated	−37.91	−34.32	95.8	1.99
Imposed	−61.92	0.12	−120	4.0
Evaluated	−61.89	0.23	−129.3	4.26

symmetric due to the memory of the shape of the body, and to not symmetric boundaries with a water–air interface on one side and a rigid wall on the opposite side.

The limited distance of the hydrofoil from the free surface also induces a breaking wave which adds vorticity to the flow field. The specific geometry assembly of the hydrofoil is responsible for a strong defect velocity in the wake with large shear and consequent huge turbulence development and vorticity. In the low pressure side of the hydrofoil a recirculation zone develops with separation, while the trailing edge injects an accelerated boundary layer in the
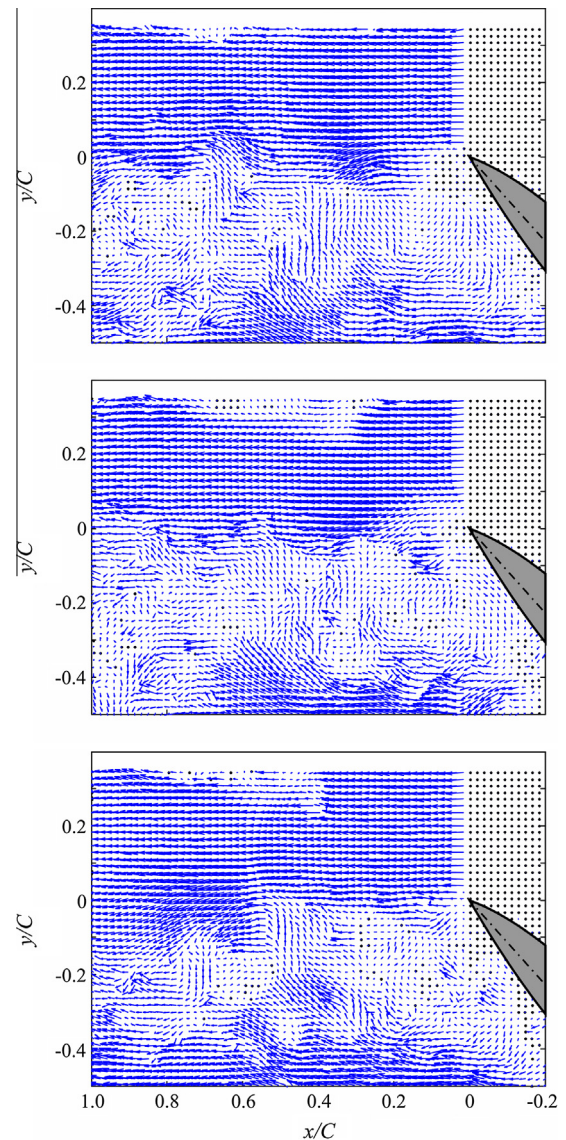

Fig. 4. Sequence of snapshots of the instantaneous measured velocity near the trailing edge. The snapshots are 0.27 s apart.

upper half of the wake. Moving downstream, the wake is progressively refilled with momentum transferred towards the axis of the wake by the strong shear and by eddies moving in the flow field. Hence the defect velocity is progressively reduced downstream, where the flow tends to recover the undisturbed configuration. The external level of turbulence can affect the growth of the wall boundary layer on the high pressure side of the hydrofoil, with a faster growth for high turbulence level. The interaction between the external (incoming free stream) and the internal turbulence (wall boundary layer; the two regions differ in their statistics such as their integral length scales) may be caused by the external turbulence being advected into the growing boundary layers or directly inducing pressure and velocity fluctuations in the boundary layer. In general, if the wall layer has a higher level of turbulence, separation due to pressure gradient is postponed since the momentum deficit in the boundary layer is smaller. In the present case this effect is negligible since the separation happens at the trailing edge, a sharp discontinuity, and is not significantly affected by the level of turbulence of the incoming boundary layer.

The free surface is oscillating with the generation of capillary waves upstream respect to the toe. It also enhances turbulence since it is breaking possibly with small quantity of air inclusion (see [25], for an extended analysis of turbulence beneath the interface in presence of small breaking waves). Fig. 5 shows a sequence of frames 1/25 s apart revealing the fluctuations of the breaker and the periodic movement of its toe.

In a self-similar wake the expected level of fluctuating velocity is $u' = 0.35\,U_s$, U_s being the defect velocity, and the expected level of shear stress is $\overline{u'v'}_{max} = -0.05U_s^2$ (see [39]). These values should be taken as order of magnitude, since most of our measurements are in the near body region were self-similarity has not yet achieved. The results shown in [26] (see Figs. 4, 5 and 7) confirm that our measurements are within the order of magnitude of the values suggested for a theoretical wake in the far field.

5. Statistics of the eddies

The distribution of the detected eddies is shown in Fig. 6 with most of the approximately 8800 detected vortex cores concentrated near the trailing edge and past the leading edge (the vortices at the leading edge and low pressure side are excluded because measurements were not performed in that area) at a distance less than $x \approx C$.

The eddies beneath the free surface are still present at $x \approx 4C$ and are mainly CW rotating. The minimum radius of the detectable vortices is fixed by the PIV mesh limits (1.81 mm in the present experiments), which do not necessarily correspond to the minimum size of the vortices present in the flow field. Willert and Gharib [42] have discussed the low-pass filtering effect of PIV due to the averaging over the Interrogation Windows, showing that the spatial cut-off wavelength is twice the window size according to the Nyquist criterion. Foucaut et al. [14], looking at the spectrum observed that the PIV behaves as a low pass filter characterised by a square sinc function with a cut off wave number equal to 2.8/X, X being the physical window size. Hence the minimum wavelength is 2.24 the window size. Since the interrogation windows is 32×32 pixels, results a minimum radius of the eddies equal to ≈ 4 mm.

The CW and CCW distributions reflect the mean vorticity distribution even though a limited number of eddies can also be found for which the mean vorticity has the opposite sign, which is a consequence of the fluctuations in the vorticity field. Decreasing the threshold increases the number of eddies because weaker vortices are included as well. The axes of the distributions are almost coincident with the edges of the wake of the foil, with the distribution in the upper lobe influenced by the breaker (see Fig. 2 for the identification of the lobes of the wake of the foil). The maximum value of the spatial probability distribution is less than 1.6% and is located near the trailing edge at small distance downstream. In fact, the videos and the photographs show that at the trailing edge, the flow still resembles the wall boundary layer and has not yet experienced the strong shear associated with the jet encountering the fluid that is almost at rest in the recirculation zone. This behaviour, with a small spatial gap between the trailing edge and the area where eddies start to appear, differs from the observations by Bourgoyne et al. [4] who, for a hydrofoil parallel to the stream, observed vortices of opposite sign convected by the wall boundary layers (on both sides of the body) and shed at the trailing edge. The
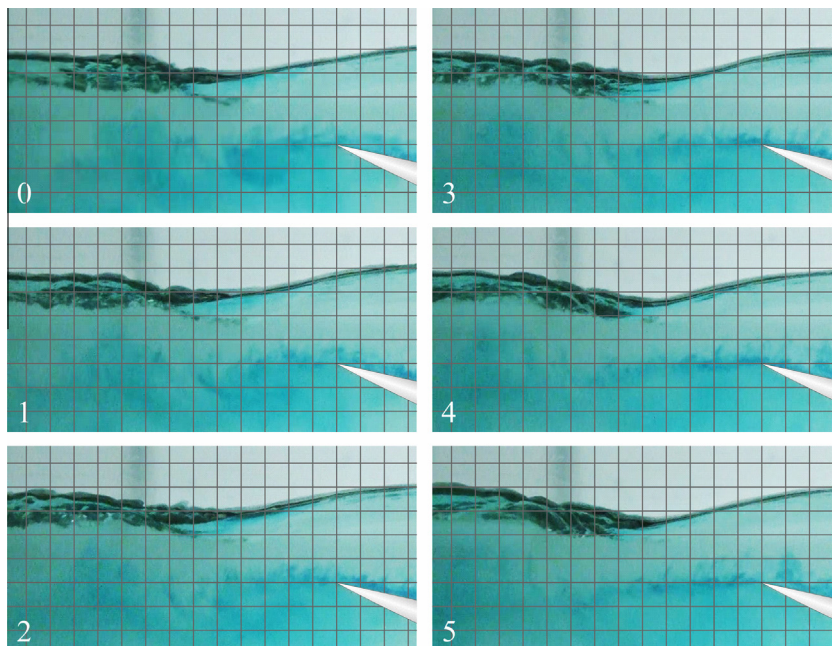

Fig. 5. Sequence of frames showing the free surface fluctuations. The grid step is 10 mm, the frames are 1/25 s apart.
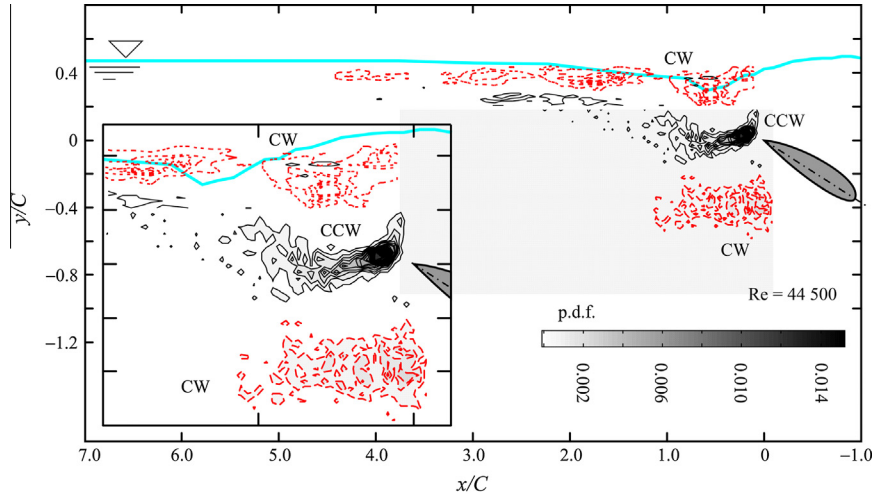
Fig. 6. The spatial probability distribution of vortices. The dashed lines refer to CW vortices. The presence of CCW vortices in the lower lobe of the wake and of CW vortices in the upper lobe of the wake is exceptional. Most vortices beneath the free surface are CW rotating.
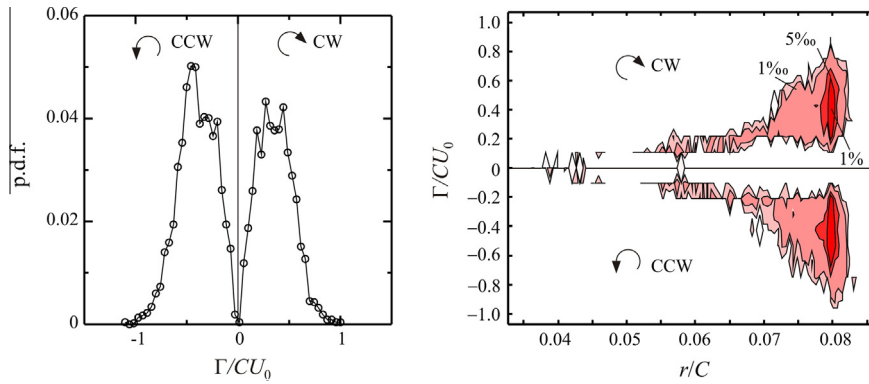

Fig. 7. The probability distribution function of the vortex core circulation (left panel) and the joint PDF of core vortex circulation and radius (right panel).

main difference is the absence of one of the two wall boundary layers in the present experiments due to flow separation in the low-pressure side.

In the left panel of Fig. 7, the probability distribution of the circulation associated with the detected vortices is shown.

The CCW vortices show a secondary peak (even though it is not well marked) and are generally more intense and numerous than the CW vortices. The right panel of the same figure shows the joint PDF of the circulation vs. the radius of the detected vortices. The larger vortices also have larger circulation and are more frequent. The asymmetry of the PDF mirrors the effects of the free surface, which affects both turbulence and eddies dynamics.

The database also contains the instantaneous level of vorticity in the core of the detected vortices. If pure vortices were filling the flow field, the following theoretical relationship between the circulation and the average vorticity, which was obtained by space averaging in the core the Eq. (10), would be rigorously satisfied:

$$\Gamma_t = \frac{\overline{\omega_z}\pi r_e^2}{1 - \exp\left(-r_e^2/2\sigma^2\right)}. \tag{10}$$

This expression is based on the detected radius r_e and σ and on the space-averaged value of vorticity $\overline{\omega_z}$ in the domain occupied by the vortex core.

Fig. 8 shows the PDF of the circulation in the detected vortices and the theoretical circulation in Eq. (10). The dashed line represents a perfect agreement. The correlation is fairly good with

limited deviations for strong circulations (typical of larger vortices) due to the background presence of vorticity not contained in eddies.

Fig. 9 is identical to Fig. 7 but refers the eddies near the free surface. Clockwise eddies are more frequent with a peak at $\Gamma/CU_0 = 0.5$.

To evaluate the role of the eddies as preferential carriers of energy and stress, we can compare the average values of the TKE and the Reynolds shear stress at the locations of the eddies and the values of the same variables conditional to the presence of the eddies (Reynolds shear stress and TKE fields are shown in [26]). The PDF for the average value is shown in the left panel of Fig. 10.

The distribution is symmetric with respect to the zero shear stress axis even for positive Reynolds shear stresses, which are associated with large values of TKE and are more frequent than negative Reynolds shear stresses (positive shear stresses are characteristics of the lower lobe wake). There are some empty regions indicating that the most frequent locations of eddies are preferentially distributed and not uniform. The joint PDF for the instantaneous values (right panel in Fig. 10) shows that the maximum values of the instantaneous TKE and the Reynolds shear stress in the presence of eddies are twice the maximum time-averaged values, i.e., the conditional average of TKE in presence of eddies is larger than the time-averaged value of TKE.

If we consider the quadrant decomposition of the time-averaged Reynolds shear stress at the location of the vortices, the four joint
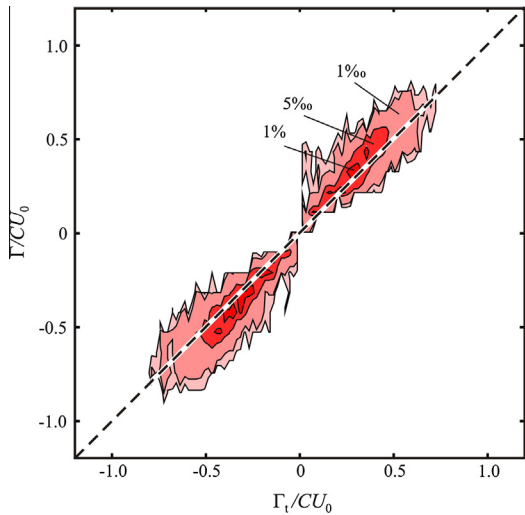
Fig. 8. The probability distribution function of the vortex core circulation and of the computed circulation based on the vorticity and on the radius of the vortices. The dashed line is the perfect agreement.

PDF with the instantaneous shear stress at the same location can be computed, as shown in Fig. 11. The computation was carried out as follows. For the horizontal axis: (i) the instantaneous value of the shear stress at the location of an eddy was stored. (ii) The values

recorded for eddies appeared at the same location were averaged in order to evaluate the conditional average of the shear stress at that location during the presence of eddies. For the vertical axis: the time average shear stress is considered for the locations of appearance of eddies. The dashed areas indicates the domain where shear stress counter-flux takes place, i.e. the shear stress associated with the eddy presence has opposite sign respect to the average shear stress. The dashed line indicates an equal level of both the stresses; hence, the area outside the triangular domain delimited by the dashed lines is the PDF of the eddies carrying higher stress with respect to the local time-averaged stress. Such eddies are usually associated with events in quadrant Q2, and the transport shear stress of an opposite sign with respect to the local mean stress exists only for the time-averaged stress less than approximately 0.05 (in absolute non dimensional value). In quadrant Q1, there is a significant presence of eddies carrying more than twice the time-averaged value. Notably, the most frequent eddies (i.e., with a larger value of the PDF) transport much less shear than the average at that location, and the maximum is at a level of 0.04 (absolute non dimensional value) of the time-averaged local shear for all quadrants. The second quadrant also has secondary maxima, and the most relevant is at 0.08.

Fig. 12 shows the same data that are shown in Fig. 11 but separating the lower and the upper lobe of the wake. Fig. 12 shows that the counter-flux eddies (transporting the Reynolds shear stress with an opposite sign with respect to the time average) in
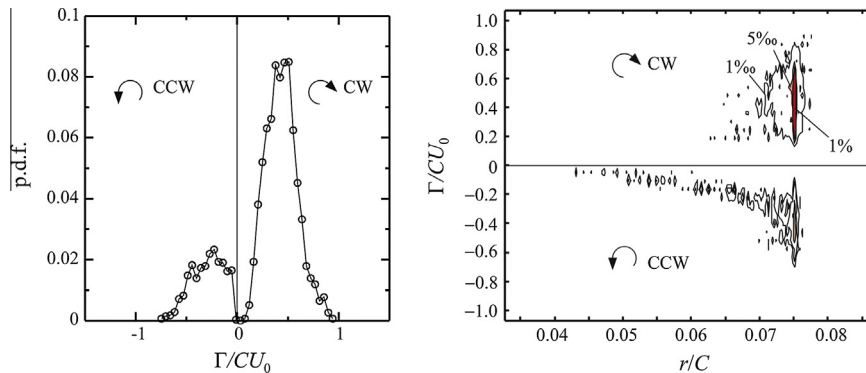

Fig. 9. The probability distribution function of the vortex core circulation (left panel) and joint PDF of vortex core circulation and radius (right panel). Eddies near the free surface.
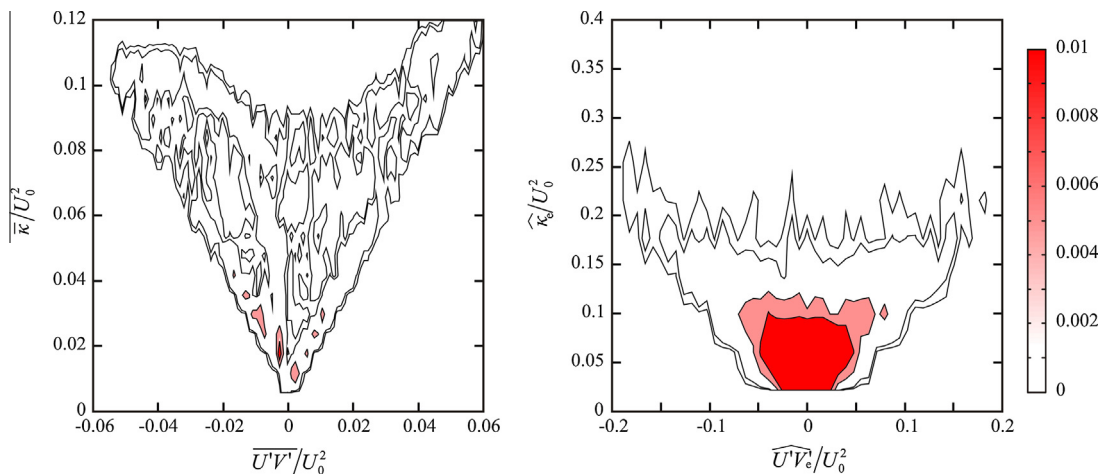

Fig. 10. The joint probability distribution function of the kinetic turbulent energy and the Reynolds shear stress. The left panel shows the time-averaged value of the flow field at the location of eddy detection; the right panel shows the instantaneous value at the same locations.
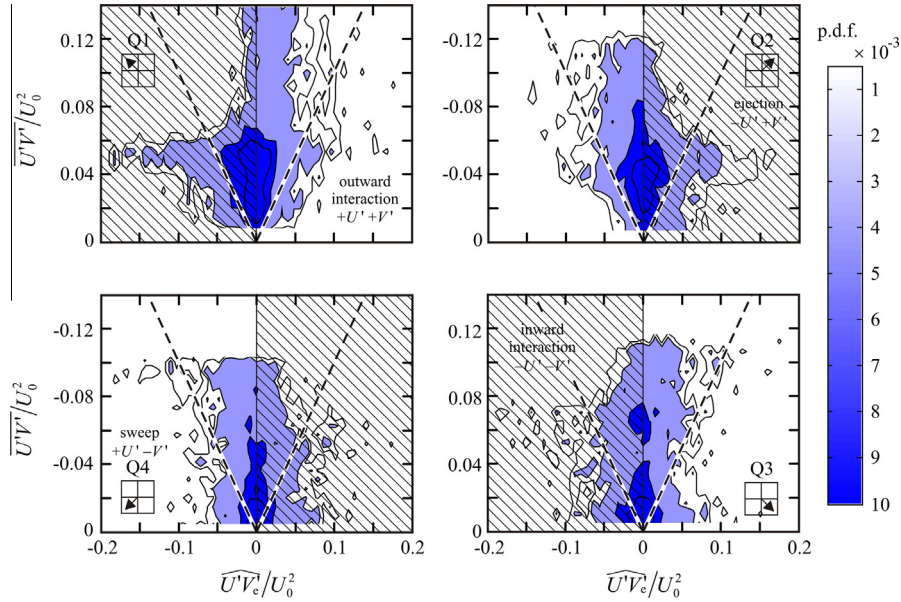
Fig. 11. The joint probability distribution function of the time-averaged Reynolds shear stress quadrant decomposed at the location of the eddies (vertical axis) and the Reynolds shear stress in presence of the eddies $\widehat{U'V'}_e$ (horizontal axis). The dashed lines limit the domain with the time-averaged stress greater than the eddy-contributed shear stress. The dashed areas limit the domain where the sign of the shear stress averaged during the eddy presence is opposite to the sign of the time average shear stress. Eddies occurring in the dashed areas transport a counter-flux shear stress. Contour lines are at 0.0005, 0.001, 0.005, 0.01.
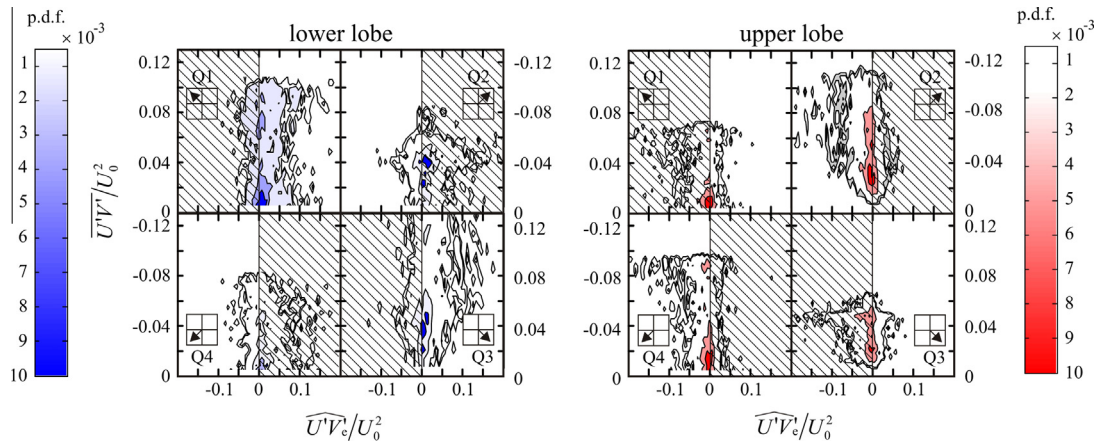

Fig. 12. See Fig. 9 for caption. The left panel refers to the lower lobe of the wake, the right panel refers to the upper lobe. Contour lines at 0.0005, 0.001, 0.005, 0.01.

the lower lobe belong to quadrant Q2 and that in the upper lobe eddies in quadrant Q3 and Q1 exhibit a similar behaviour.

A further conditional statistic includes the sign of circulation as well. Table 3 reports the ratio between the shear stress contribution due to eddies with respect to the mean shear stress at the location of the eddies, which is averaged over all the frames.

The negative sign in Table 3 refers to eddies that have an average transport shear with an opposite sign with respect to the quadrant decomposed time-averaged value. This negative transport represents a counter-flux with respect to the average flux, but

there are few corresponding vortices, as can be observed in the spatial joint PDF of the Production of TKE conditionally evaluated in the presence of the eddies (not shown). Events Q2 and Q4 are dominant in the upper lobe of the wake of the foil where almost all eddies are counter-clockwise; events Q1 and Q3 are dominant in the lower lobe of the wake where almost all eddies are clockwise.

6. Conditional contribution to the TKE balance equation in the presence of the eddies

The most general expression of the balance equation for the TKE is [39]

Table 3
Ratio of the shear stress associated with eddy location and of the time-averaged quadrant decomposed shear stress at the same location. The shear stress associated with the eddies is decomposed with respect to the sign of the circulation.

	Q1	Q2	Q3	Q4
CW	0.36	−0.45	0.28	−0.46
CCW	−0.43	0.27	−0.36	0.35

$$\underbrace{-\overline{U_i'U_j'}S_{ij}}_{P=production} \underbrace{-\overline{U}_i\frac{\partial\left(\overline{q^2/2}\right)}{\partial x_i}}_{A=advection} - \frac{\partial}{\partial x_i}\underbrace{\left(\frac{1}{\rho}\overline{p'U_i'}+\overline{q^2U_i'/2}-2\nu\overline{U_i's_{ij}}\right)}_{T=transport} - \underbrace{2\nu\overline{s_{ij}s_{ij}}}_{D=dissipation} = 0,$$

(11)

where $q^2 = \overline{U'_i U'_i}$ is two times the kinetic energy per unit mass, $S_{ij} = \frac{1}{2}\left(\frac{\partial \overline{U}_i}{\partial x_j} + \frac{\partial \overline{U}_j}{\partial x_i}\right)$, $i,j = 1,2,3$ is the mean strain rate, $s_{ij} = \frac{1}{2}\left(\frac{\partial U'_i}{\partial x_j} + \frac{\partial U'_j}{\partial x_i}\right)$, $i,j = 1,2,3$ is the fluctuating strain rate, v is the kinematic viscosity, and ρ is the mass density. For the present experiments, the third component of the velocity is missing and Eq. (11) is simplified accordingly.

In the following, the terms of the TKE balance equations shall be quantified in a sub domain collecting the instantaneous data only during the presence of an eddy, and space averaging will be performed over the core of the eddy. A comparison is made using (1) the conditional analysis of the instantaneous values; (2) the conditional analysis of the time averaged values (this last is a spatial average of the time averaged values over the extension of the same eddy). Note that this conditional analysis does not imply that the eddies are effectively carrying the various contributions (e.g., the terms $U'_i U'_j$ in the production term) but simply the assumption that the presence of an eddy can significantly change locally some variables of the flow field.

According to these assumptions, the production in the presence of the eddies is expressed as

$$\widehat{P}_{eij} = -\frac{1}{N_e}\sum_{k=1}^{N_e}\frac{\int_{S_k} U'_i U'_j \frac{\partial(\overline{U}_i)}{\partial x_j}\,dS}{S_k}, \tag{12}$$

where the correlation $U'_i U'_j$ is the instantaneous value during the kth eddy presence. The integral is extended to the core S_k of the kth eddy, and the sum is extended to the N_e detected eddies. The production of the time-averaged flow in the domain occupied by the eddies is

$$\overline{P}_{ij} = -\frac{1}{N_e}\sum_{k=1}^{N_e}\frac{\int_{S_k} \overline{U'_i U'_j} \frac{\partial(\overline{U}_i)}{\partial x_j}\,dS}{S_k}, \tag{13}$$

where with respect to Eq. (12), the Reynolds stress components are the time-averaged value, i.e., refer to the mean flow.

The joint PDF of the two variables is shown in Fig. 13 separately for the eddies in the wake of the foil (left panel) and for the eddies beneath the free surface (right panel).

The results are listed in Table 4. The eddies in the wake of the foil occasionally are associated with a loss of TKE (not necessarily a transfer from the eddies to the mean flow because transport and advection are also present), but as shown in Table 4, last column, the overall balance is a net production of TKE. Beneath the free surface, the sign of the distribution is less anisotropic but still has a positive net value.

In the wake of the foil, the negative contribution is due to the acceleration of the mean longitudinal velocity due to the reduction of the velocity defect at the expense of the fluctuating longitudinal component because $U'U'$ is positive definite. The maximum positive value is represented by term P_{12}, where the Reynolds shear stress couples with the mean shear associated to the longitudinal velocity variation in the vertical.

Beneath the free surface, the main TKE production term is P_{11}, which corresponds to the transfer of energy to turbulence due to the deceleration of the mean longitudinal velocity. It is expected that in a thin layer beneath the free surface, the sign of this contribution becomes negative because the longitudinal velocity is mainly accelerated herein [10].

In the wake the total production in the presence of the eddies, equal to 0.071, is approximately 15% stronger than the time average at the same location occupied by the eddies, equal to 0.062. Beneath the free surface, the total production is approximately 30% weaker than the time average. The relative reduction beneath the free surface can be addressed to the strong shear generated by the roller, which is responsible for most of the turbulent energy production but with very limited generation of eddies.

A similar analysis has been carried out for the advection. The advection in the presence of eddies is
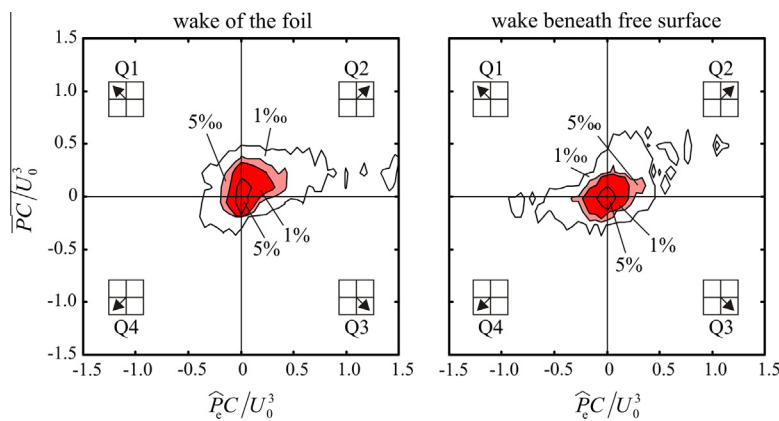

Fig. 13. The joint PDF of the production of TKE conditionally evaluated in the presence of the eddies. The left panel refers to the eddies in the wake, and the right panel refers to the eddies near the free surface. The contour lines are at 0.001, 0.005, 0.01.

Table 4
Contribution of the eddies and of the average flow to the TKE production.

	$\widehat{P}_{e11}C/U_0^3, \overline{P}_{11}C/U_0^3$	$\widehat{P}_{e22}C/U_0^3, \overline{P}_{22}C/U_0^3$	$\widehat{P}_{e12}C/U_0^3, \overline{P}_{12}C/U_0^3$	$\widehat{P}_{e21}C/U_0^3, \overline{P}_{21}C/U_0^3$	$\widehat{P}_e C/U_0^3, \overline{P}C/U_0^3$
Wake of the foil					
Eddies	−0.058	0.017	0.115	−0.003	0.071
Average flow	−0.056	0.022	0.097	−0.002	0.062
Free surface					
Eddies	0.024	0	0.002	0	0.025
Average flow	0.027	0	0.009	0	0.035

$$\widehat{A}_{1e} = -\frac{1}{N_e}\sum_{k=1}^{N_e}\frac{\int_{S_k}\overline{U}\frac{\partial(1/2q^2)}{\partial x}dS}{S_k}, \quad \widehat{A}_{2e} = -\frac{1}{N_e}\sum_{k=1}^{N_e}\frac{\int_{S_k}\overline{V}\frac{\partial(1/2q^2)}{\partial y}dS}{S_k},$$

$$\widehat{A}_e = \widehat{A}_{1e} + \widehat{A}_{2e},$$

(14)

and the advection of the time-averaged flow at the same location of the eddies is

$$\overline{A}_1 = -\frac{1}{N_e}\sum_{k=1}^{N_e}\frac{\int_{S_k}\overline{U}\frac{\partial\left(\overline{1/2q^2}\right)}{\partial x}dS}{S_k}, \quad \overline{A}_2 = -\frac{1}{N_e}\sum_{k=1}^{N_e}\frac{\int_{S_k}\overline{V}\frac{\partial\left(\overline{1/2q^2}\right)}{\partial y}Ds}{S_k},$$

$$\overline{A} = \overline{A}_1 + \overline{A}_2.$$

(15)

The results are listed in Table 5.

In the wake of the foil, the dominant term is $\widehat{A}_{1e}$, which is associated with a reduction in the TKE in the streamwise direction and the total advection in the presence of eddies is an order of magnitude greater than the advection due to the time-averaged flow at the same location. It confirms the important role of eddies in the overall dynamics of turbulence in the present flow field.

Another contribution to the TKE balance is the transport term due to turbulence itself. The two other transport contributions due to viscosity and to fluctuating pressure are usually neglected. The first is neglected because it is order of magnitude less than the other terms, and the second is neglected because it is extremely difficult to measure it directly with an acceptable uncertainty. In a two-dimensional flow, the transport of the turbulence due to turbulence contains only four terms, namely

$$T_{11} = -\frac{\partial}{\partial x}\left(\overline{\frac{1}{2}U'^2U'}\right), \quad T_{12} = -\frac{\partial}{\partial y}\left(\overline{\frac{1}{2}U'^2V'}\right)$$

$$T_{21} = -\frac{\partial}{\partial x}\left(\overline{\frac{1}{2}V'^2U'}\right), \quad T_{22} = -\frac{\partial}{\partial y}\left(\overline{\frac{1}{2}V'^2V'}\right),$$

(16)

which can be collected in two terms:

$$T_1 = -\frac{\partial}{\partial x}\left(\overline{\frac{1}{2}q^2U'}\right), \quad T_2 = -\frac{\partial}{\partial y}\left(\overline{\frac{1}{2}q^2V'}\right).$$

(17)

As for the other contributions to the TKE balance equation, the transport is also evaluated through a conditional averaging during the presence of eddies:

$$\widehat{T}_{1e} = -\frac{1}{N_e}\sum_{k=1}^{N_e}\frac{\int_{S_k}\frac{\partial(1/2q^2U')}{\partial x}dS}{S_k}, \quad \widehat{T}_{2e}$$

$$= -\frac{1}{N_e}\sum_{k=1}^{N_e}\frac{\int_{S_k}\frac{\partial(1/2q^2V')}{\partial y}dS}{S_k}.$$

(18)

In a similar way, the conditional average is applied to the average flow field, obtaining

$$\overline{T}_1 = -\frac{1}{N_e}\sum_{k=1}^{N_e}\frac{\int_{S_k}\frac{\partial\left(\overline{1/2q^2U'}\right)}{\partial x}dS}{S_k}, \quad \overline{T}_2 = -\frac{1}{N_e}\sum_{k=1}^{N_e}\frac{\int_{S_k}\frac{\partial\left(\overline{1/2q^2V'}\right)}{\partial y}dS}{S_k}.$$

(19)

Table 5
Contribution of the eddies and of the average flow to the advection of the TKE.

Wake of the foil			
Eddies	$\widehat{A}_{1e}C/U_0^3 = 0.054$	$\widehat{A}_{2e}C/U_0^3 = -0.014$	$\widehat{A}_eC/U_0^3 = 0.040$
Average flow	$\overline{A}_1C/U_0^3 = 0.013$	$\overline{A}_2C/U_0^3 = -0.017$	$\overline{A}C/U_0^3 = -0.004$
Free surface			
Eddies	$\widehat{A}_{1e}C/U_0^3 = 0.049$	$\widehat{A}_{2e}C/U_0^3 = 0.001$	$\widehat{A}_eC/U_0^3 = 0.050$
Average flow	$\overline{A}_1C/U_0^3 = 0.023$	$\overline{A}_2C/U_0^3 = -0.007$	$\overline{A}C/U_0^3 = 0.016$

Table 6
Contribution of the eddies and of the average flow to the TKE transport due to turbulence.

Wake of the foil			
Eddies	$\widehat{T}_{1e}C/U_0^3 = -0.084$	$\widehat{T}_{2e}C/U_0^3 = 0.053$	$\widehat{T}_eC/U_0^3 = -0.031$
Average flow	$\overline{T}_1C/U_0^3 = 0.016$	$\overline{T}_2C/U_0^3 = -0.016$	$\overline{T}C/U_0^3 = 0$
Free surface			
Eddies	$\widehat{T}_{1e}C/U_0^3 = -0.058$	$\widehat{T}_{2e}C/U_0^3 = 0.014$	$\widehat{T}_{2e}C/U_0^3 = -0.044$
Average flow	$\overline{T}_1C/U_0^3 = -0.022$	$\overline{T}_2C/U_0^3 = -0.003$	$\overline{T}C/U_0^3 = -0.025$

Table 7
Contribution of the eddies and of the average flow to the TKE production plus advection and transport.

	$(P+A+T)C/U_0^2$
Wake of the foil	
Eddies	0.080
Average flow	0.058
Free surface	
Eddies	0.031
Average flow	0.026

In Table 6, the results for the two separate domains, the wake of the foil and the flow beneath the free surface, are shown.

In the wake of the foil, the net transport is negligible considering the average flow, whereas it is negative during the presence of eddies. Near the free surface in the presence of eddies, the transport is much stronger than the average value and is negative.

The missing terms in this analysis are the dissipation and the transport due to the fluctuating pressure because in both cases, the uncertainty in the experimental evaluation is very high. Summing the three terms results in the value listed in Table 7.

The closure of the balance requires a dissipation term equal to these values, with the inclusion of the transport contribution due to the fluctuating pressure.

7. Conclusion

The flow velocity in the field generated by a hydrofoil beneath an air–water interface has been experimentally measured with a DPIV and further analysed with a specific attention to coherent structures detection (mainly eddies).

- The small eddies are identified using a continuous wavelet transform of the vorticity field. An original procedure has been developed and applied for the optimal evaluation of the geometric characteristics of the small eddies and of their location.
- The detected eddies have been analysed to evaluate their spatial distribution and their intensity separating the wake of the foil-related from the breaker-related eddies. The wake of the foil-related eddies have an almost symmetric distribution at the core circulation, with a slight dominance of CCW eddies. The peaks are at $\Gamma/CU_0 \approx \pm 0.5$ and the bigger eddies are usually associated with strong circulation. The breaker-related eddies show an asymmetric distribution of the core circulation, and CW eddies are dominant. The peak is still at $\Gamma/CU_0 \approx 0.5$ even though the proper length scale could be the breaker height instead of the cord length.
- The free surface has the effect of breaking the symmetry of the wake also modifying the eddies dynamics and interactions in the upper lobe of the wake. It is also a source of TKE and of vorticity, both affecting the dynamics and the energy in the upper lobe of the wake and the eddies herein located.

- The joint PDF of the turbulent kinetic energy and the Reynolds shear stress is computed by using the time-averaged values in the area occupied by the eddies. The PDF is almost symmetric with respect to the zero shear stress, even though large values of the TKE are more frequently associated with positive Reynolds shear stress. A similar PDF for the instantaneous values during the presence of eddies shows values of both variables roughly twice the average values, i.e., eddies are associated with larger turbulence fluctuations of the flow field with respect to the time-averaged flow field.

- The joint PDF of the time-averaged Reynolds shear stress and of the instantaneous shear stress in the area occupied by the eddies, with the conditional statistics of the quadrants, shows that eddies usually carry shear stress of the same sign as the time-averaged stress, but specifically, they carry stress of an opposite sign. This scenario occurs more frequently for events in quadrant Q2 with eddies transporting positive shear stress in the presence of a negative time-averaged value. In quadrant Q1, there is a significant presence of eddies carrying more than twice the time-averaged value. The statistics with a separation of the eddies in the lower and the upper lobe of the wake show that the counter-flux eddies (transporting Reynolds shear stress with an opposite sign respect to the time average) for quadrant Q2 belong to the lower lobe and that the upper lobe has eddies in quadrant Q3 with a similar behaviour.

- The conditional statistics of the Reynolds shear stress quadrant decomposed during the presence of the eddies indicates that the presence of the eddies results in a lower value of the Reynolds shear stress (less than 50% with respect to the time-averaged values at the location occupied by the eddies). The sign of the Reynolds shear stress is systematically opposite to the time-averaged value in quadrant Q2–Q4 for CW eddies and in quadrants Q1–Q3 for CCW eddies. Therefore, in presence of the eddies there is a counter-flux of momentum.

- The conditional analysis of the terms of the TKE balance indicates that, in the wake of the foil, during the presence of eddies, the production is ≈15% greater than the time-averaged production at the same location occupied by the eddies. Beneath the free surface, the production is ≈30% weaker than the time average. This last value can be explained by the strong shear generated by the breaker, which is responsible for most of the turbulent energy production without a corresponding strong presence of eddies. A similar analysis for the advection indicates that, in the wake of the foil, the advection in the presence of eddies is an order of magnitude greater (in absolute value) than the advection due to the time-averaged flow at the same location. Additionally, beneath the free surface, advection in the presence of the eddies is much greater than the average. A similar behaviour can be observed for the transport term due to turbulence. Therefore, in the presence of eddies, the production plus advection plus transport is enhanced with respect to the average flow, which is approximately 40% in the wake of the foil and 20% beneath the free surface.

- It is left to future work the unambiguous validation of the proposed model possibly with a synthetized turbulence flow field possibly obtained by direct numerical simulation of the Navier–Stokes equation and filled with eddies. Another important development is the separation of the Reynolds stresses due to eddies from Reynolds stresses due to uncoherent turbulence. This last goal is essential in order to quantify the real contribution of eddies (amongst all the possible coherent structures) to the transport mechanisms in the flow field. The extension of the analysis to other coherent structures should be also pursued.

References

[1] R.J. Adrian, K.T. Christensen, Z.-C. Liu, Analysis and interpretation of instantaneous turbulent velocity fields, Exp. Fluids 29 (2000) 275–290.

[2] A. Agrawal, A.K. Prasad, Properties of vortices in the self similar turbulent jet, Exp. Fluids 33 (2002) 565–577.

[3] F. Blackwelder, On the role of phase information in conditional sampling, Phys. Fluids 20 (1977) S232–S242.

[4] D.A. Bourgoyne, S.L. Ceccio, D.R. Dowling, Vortex shedding from a hydrofoil at high Reynolds number, J. Fluid Mech. 531 (2005) 293–324.

[5] R. Camussi, Coherent structure identification from wavelet analysis of particle image velocimetry data, Exp. Fluids 32 (2002) 76–86.

[6] J. Carlier, M. Stanislas, Experimental study of eddy structures in a turbulent boundary layer using particle image velocimetry, J. Fluid Mech. 535 (2005) 143–188.

[7] M.S. Chong, A.E. Perry, B.J. Cantwell, A general classification of three-dimensional flow field, Phys. Fluids A 2 (1990) 765–777.

[8] R. Cucitore, M. Quadrio, A. Baron, On the effectiveness and limitations of local criteria for the identification of a vortex, Eur. J. Mech. B/Fluids 18 (1999) 261–282.

[9] P. Chakraborty, S. Balachandar, R.J. Adrian, On the relationships between local vortex identification schemes, J. Fluid Mech. 535 (2005) 189–214.

[10] D. Dabiri, M. Gharib, Experimental investigation of the vorticity generation within a spilling water wave, J. Fluid Mech. 330 (1997) 113–139.

[11] M. Daskovsky, The hydrofoil in surface proximity, theory and experiments, Ocean Eng. 27 (2000) 1129–1159.

[12] M. Farge, Wavelet transforms and their applications to turbulence, Annu. Rev. Fluid Mech. 24 (1992) 395–457.

[13] H.E. Fiedler, Coherent structures, in: G. Comte-Bellot, J. Mathieu (Eds.), Proceedings of the First European Turbulence Conference, Lyon, France, Springer-Verlag, New York, Berlin, Heidelberg, 1987, pp. 320–336.

[14] J.M. Foucaut, J. Carlier, M. Stanislas, PIV optimization for the study of turbulent flow using spectral analysis, Meas. Sci. Technol. 15 (6) (2004) 1046.

[15] J.P. Giesing, M.O. Smith, Potential flow about two-dimensional hydrofoils, J. Fluid Mech. 28 (1) (1967) 113–129.

[16] L. Graftieaux, M. Michard, N. Grosjean, Combining PIV, POD and vortex identification algorithms for the study of unsteady turbulent swirling flows, Meas. Sci. Technol. 12 (2001) 1422–1429.

[17] G. Haller, An objective definition of a vortex, J. Fluid Mech. 525 (2005) 1–26.

[18] J.C.R. Hunt, A.A. Wray, P. Moin, Eddies, Stream, and Convergence Zones in Turbulent Flows, Center for Turbulence Research Report CTR-S88, 1988, pp. 193–208.

[19] A.K.M.F. Hussain, Coherent structures and turbulence, J. Fluid Mech. 173 (1986) 303–356.

[20] J. Jeong, A.K.M.F. Hussain, On the identification of a vortex, J. Fluid Mech. 285 (1995) 69–94.

[21] Y.-H. Kim, C. Cierpka, S.T. Wereley, Flow field around a vibrating cantilever: coherent structure eduction by continuous wavelet transform and proper orthogonal decomposition, J. Fluid Mech. 669 (2011) 584–606.

[22] S. Longo, Turbulence under spilling breakers using wavelets, Exp. Fluids 34 (2003) 181–191.

[23] S. Longo, The effects of air bubbles on ultrasound velocity measurements, Exp. Fluids 41 (4) (2006) 593–602.

[24] S. Longo, Vorticity and intermittency within the pre-breaking region of spilling breakers, Coast. Eng. 56 (2009) 285–296.

[25] S. Longo, Wind-generated water waves in a wind tunnel: free surface statistics wind friction and mean air flow properties, Coast. Eng. 61 (2012) 27–41.

[26] S. Longo, L. Chiapponi, M. Clavero, Experimental analysis of the coherent structures and turbulence past a hydrofoil in stalling condition beneath a water–air interface, Eur. J. Mech. B/Fluids 43 (2014) 172–182.

[27] H.J. Lugt, The dilemma of defining a vortex, in: U. Muller, K.G. Roesner, B. Schmidt (Eds.), Recent Developments in Theoretical and Experimental Fluid Mechanics, 1979, pp. 309–321.

[28] S. Mallat, A theory for multiresolution signal decomposition: the wavelet representation, Trans. IEEE: PAMI 11 (1989) 674–693.

[29] C. Meneveau, Analysis of turbulence in the orthonormal wavelet representation, J. Fluid Mech. 232 (1991) 469–520.

[30] A. Okubo, Horizontal dispersion of floatable trajectories in the vicinity of velocity singularities such as convergencies, Deep-Sea Res. 17 (1970) 445–454.

[31] B.R. Parkin, B. Perry, T.Y.-T. Wu, Pressure distribution on a hydrofoil running near the water surface, J. Appl. Phys. 27 (3) (1956) 232–240.

[32] A.E. Perry, M.S. Chong, A description of eddying motions and flow patterns using critical-point concepts, Annu. Rev. Fluid Mech. 19 (1987) 125–155.

[33] M. Raffel, C.E. Willert, S.T. Wereley, J. Kompenhans, Particle Image Velocimetry. A Practical Guide, Springer, 2007.

[34] S.K. Robinson, S.J. Kline, P.R. Spalart, Quasi-coherent structures in the turbulent boundary layer – II: verification and new information from a numerically simulated flat-plate boundary layer, in: S.J. Kline, N.H. Afgan (Eds.), Near Wall Turbulence. Proceedings of Zaric Memorial Conference, Hemisphere, New York, 1989, pp. 218–247.

[35] E. Roohi, A.P. Zahiri, M. Passandideh-Fard, Numerical simulation of cavitation around a two-dimensional hydrofoil using VOF method and LES turbulence model, Appl. Math. Model. 37 (2013) 6469–6488.

[36] C. Schram, P. Rambaud, M.L. Riethmuller, Wavelet based eddy structure eduction from a backward facing step flow investigated using particle image velocimetry, Exp. Fluids 36 (2004) 233–245.

[37] A.-M. Shinneeb, A. Pollard, Identification of vortical structures inside the human pharynx/larynx region from POD-reconstructed velocity fields, Exp. Fluids 53 (2012) 353–367.

[38] M. Tabor, I. Klapper, Stretching and alignment in chaotic and turbulent flows, Chaos Solitons Fract. 4 (1994) 1031–1055.

[39] H. Tennekes, J.L. Lumley, A First Course in Turbulence, MIT Press, 1972.

[40] J. Weiss, The dynamics of enstrophy transfer in 2-dimensional hydrodynamics, Physica D 48 (1991) 273–294.

[41] I.J. Wygnanski, F.H. Champagne, On transition in a pipe. Part I. The origin of puffs and slugs and the flow in a turbulent slug, J. Fluid Mech. 59 (1973) 281–335.

[42] C.E. Willert, M. Gharib, Digital particle image velocimetry, Exp. Fluids 10 (1991) 181–193.

[43] J. Zhou, R.J. Adrian, S. Balachandar, T.M. Kendall, Mechanisms for generating coherent packets of hairpin vortices, J. Fluid Mech. 387 (1999) 353–396.